

# Insights into the subsurface structure of the Caloris basin, Mercury, from assessments of mechanical layering and changes in long-wavelength topography

Christian Klimczak,<sup>1</sup> Carolyn M. Ernst,<sup>2</sup> Paul K. Byrne,<sup>1</sup> Sean C. Solomon,<sup>1,3</sup>  
Thomas R. Watters,<sup>4</sup> Scott L. Murchie,<sup>2</sup> Frank Preusker,<sup>5</sup> and Jeffrey A. Balcerski<sup>6</sup>

Received 15 June 2013; revised 7 September 2013; accepted 11 September 2013; published 3 October 2013.

[1] The volcanic plains that fill the Caloris basin, the largest recognized impact basin on Mercury, are deformed by many graben and wrinkle ridges, among which the multitude of radial graben of Pantheon Fossae allow us to resolve variations in the depth extent of associated faulting. Displacement profiles and displacement-to-length scaling both indicate that faults near the basin center are confined to a ~4-km-thick mechanical layer, whereas faults far from the center penetrate more deeply. The fault scaling also indicates that the graben formed in mechanically strong material, which we identify with dry basalt-like plains. These plains were also affected by changes in long-wavelength topography, including undulations with wavelengths of up to 1300 km and amplitudes of 2.5 to 3 km. Geographic correlation of the depth extent of faulting with topographic variations allows a first-order interpretation of the subsurface structure and mechanical stratigraphy in the basin. Further, crosscutting and superposition relationships among plains, faults, craters, and topography indicate that development of long-wavelength topographic variations followed plains emplacement, faulting, and much of the cratering within the Caloris basin. As several examples of these topographic undulations are also found outside the basin, our results on the scale, structural style, and relative timing of the topographic changes have regional applicability and may be the surface expression of global-scale interior processes on Mercury.

**Citation:** Klimczak, C., C. M. Ernst, P. K. Byrne, S. C. Solomon, T. R. Watters, S. L. Murchie, F. Preusker, and J. A. Balcerski (2013), Insights into the subsurface structure of the Caloris basin, Mercury, from assessments of mechanical layering and changes in long-wavelength topography, *J. Geophys. Res. Planets*, 118, 2030–2044, doi:10.1002/jgre.20157.

## 1. Introduction

[2] The Caloris basin, with a diameter of ~1550 km the largest well-preserved impact basin on Mercury (Figure 1a) [Murchie et al., 2008], preserves a complex tectonic history. The interior of the basin is filled with smooth volcanic plains units [Murray et al., 1975; Strom et al., 1975; Trask and

Additional supporting information may be found in the online version of this article.

<sup>1</sup>Department of Terrestrial Magnetism, Carnegie Institution of Washington, Washington, D.C., USA.

<sup>2</sup>The Johns Hopkins University Applied Physics Laboratory, Laurel, Maryland, USA.

<sup>3</sup>Lamont-Doherty Earth Observatory, Columbia University, Palisades, New York, USA.

<sup>4</sup>Center for Earth and Planetary Studies, National Air and Space Museum, Smithsonian Institution, Washington, D.C., USA.

<sup>5</sup>German Aerospace Center, Institute of Planetary Research, Berlin, Germany.

<sup>6</sup>Department of Earth, Environmental, and Planetary Sciences, Case Western Reserve University, Cleveland, Ohio, USA.

Corresponding author: C. Klimczak, Department of Terrestrial Magnetism, Carnegie Institution of Washington, 5241 Broad Branch Road, N.W., Washington, DC 20015-1305, USA. (cklimczak@ciw.edu)

©2013. American Geophysical Union. All Rights Reserved.  
2169-9097/13/10.1002/jgre.20157

Guest, 1975; Murchie et al., 2008; Watters et al., 2009a], which, after their emplacement, were subjected to extensional and contractional brittle deformation as well as changes in long-wavelength topography [Zuber et al., 2012]. The brittle deformation is evident by the juxtaposition of normal- and thrust-fault-related landforms [Strom et al., 1975; Melosh and McKinnon, 1988; Watters et al., 2005, 2009a; Murchie et al., 2008].

[3] The Mercury Dual Imaging System (MDIS) [Hawkins et al., 2007] on the MErcury Surface, Space ENvironment, GEochemistry, and Ranging (MESSENGER) spacecraft acquired the first full images of the Caloris basin during its initial Mercury flyby in 2008. MDIS data revealed that the basin's interior smooth volcanic plains units have spectral properties distinct from those of plains units exterior to the basin [Murchie et al., 2008; Robinson et al., 2008]. Further, spectral differences within the Caloris smooth plains were found to be present in ejecta blankets, floors, and central peaks of several impact craters, suggesting that those impacts had excavated distinct material from depth [Murchie et al., 2008; Ernst et al., 2010]. From estimates of the excavation depths of spectrally distinct materials exposed in crater deposits, Ernst et al. [2010] derived a stratigraphy for several plains-covered areas on Mercury and concluded that the interior plains in the central part of the Caloris basin are between 2.5 and 4 km thick.

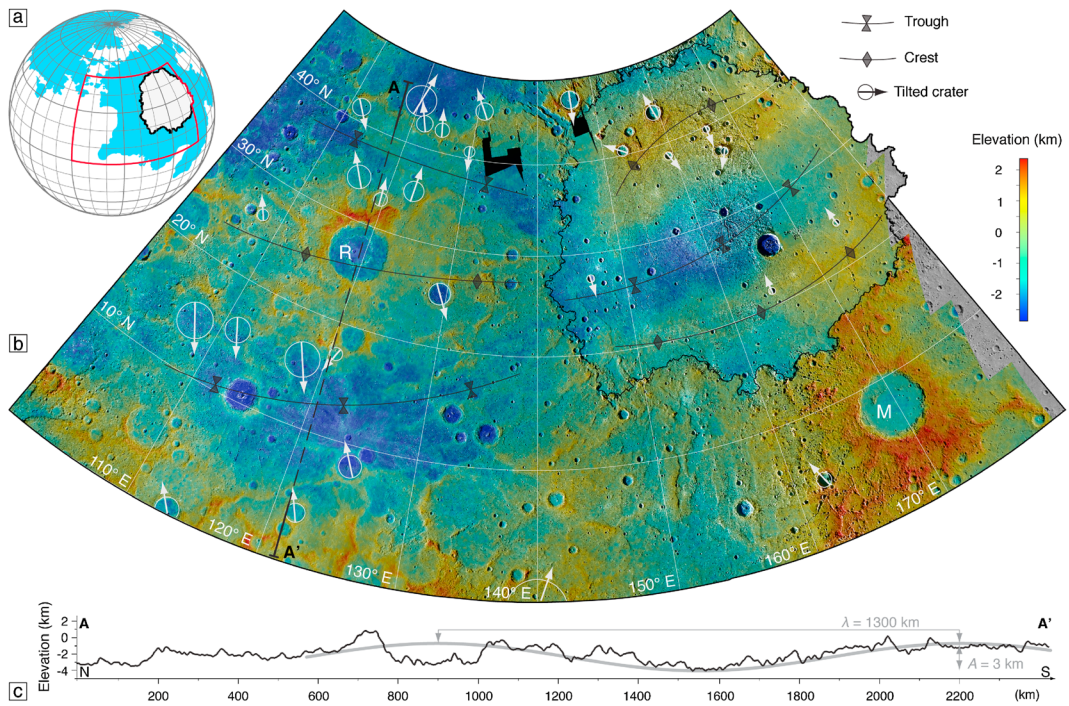


**Figure 1.** Overview of the Caloris basin area. (a) Location of the Caloris basin (black outline) relative to major expanses of smooth plains on Mercury (shown in blue, modified from Denevi *et al.* [2013]). (b) Digital terrain model (DTM) of the topography [Preusker *et al.*, 2011] of the Caloris basin and the region to its west overlaid on a Mercury Dual Imaging System (MDIS) monochrome base map, in north polar stereographic projection centered at 140°E. Indicated in white are craters that show a notable tilt of their floors; arrows indicate the direction of tilt, but arrow length does not scale to tilt amount. The systematic tilts of crater floors away from topographic highs constrain the timing of long-wavelength topographic undulations and assist in the mapping of crests and troughs. M = Mozart basin; R = Raditladi basin. The location of the profile in Figure 1c is shown as a black, partially dashed line. (c) Profile A–A' shows that topographic undulations can be approximately represented by a sinusoidal curve with a wavelength of 1300 km and an amplitude of 3 km.

[4] Stereophotogrammetric analysis of MESSENGER flyby images yielded the first topographic information for the Caloris basin [Oberst *et al.*, 2010] and revealed long-wavelength undulations of the basin floor (Figure 1b). Orbital observations with MESSENGER's Mercury Laser Altimeter (MLA) instrument [Cavanaugh *et al.*, 2007] confirmed these long-wavelength topographic undulations [Zuber *et al.*, 2012] and documented that the floors of several young, flat-floored impact craters within and around the basin are not horizontal but instead tilt in the same direction as the regional trend of the long-wavelength topography (Figure 1). These observations suggest that topographic changes affected the area in and outside the basin after the emplacement of the plains, with parts of the basin interior units displaced to elevations greater than those of the basin rim.

[5] After their emplacement, the Caloris interior smooth plains were affected by extensional and compressional tectonic stresses, manifest by the many normal- and thrust-fault-related landforms throughout the basin (i.e., graben and wrinkle ridges). Images returned by the Mariner 10 spacecraft, which viewed less than half of the basin, showed wrinkle ridges with orientations both radial and concentric to the basin center, as well as graben of no preferred orientation that outline polygonal blocks in the plains [Strom *et al.*, 1975; Melosh and McKinnon, 1988; Thomas *et al.*, 1988; Watters *et al.*, 2005].

The first MESSENGER flyby revealed graben of basin-radial and -concentric orientations [Murchie *et al.*, 2008], including the prominent complex of radial graben in the center of the basin, now named Pantheon Fossae. There is no consensus yet for the origin of Pantheon Fossae [Head *et al.*, 2008, 2009; Freed *et al.*, 2009; Watters *et al.*, 2009a; Klimczak *et al.*, 2010], but the fault geometric analysis of Klimczak *et al.* [2010] suggested that the graben-bounding faults are vertically confined to stratigraphic or mechanical units in the central Caloris basin.

[6] Orbital images with substantially improved lighting geometry and resolution (Figures 2 and 3) now permit an in-depth mechanical analysis of the faults of the Pantheon Fossae graben. Such fault analysis can improve the characterization of the depth extent of faulting throughout the Caloris basin and can test whether there is a vertical confinement of the graben in the basin center. Information on the depth extent of faulting and the confinement of the faults to mechanical or stratigraphic layering provides insight into the emplacement of the interior volcanic plains as well as the timing and processes involved in the changes in long-wavelength topography across the region. In this paper we characterize the shapes of the graben-bounding faults within the Caloris basin in terms of their lengths and displacements, infer the depth extent of faulting, and compare these results to the topography within and surrounding the Caloris basin.

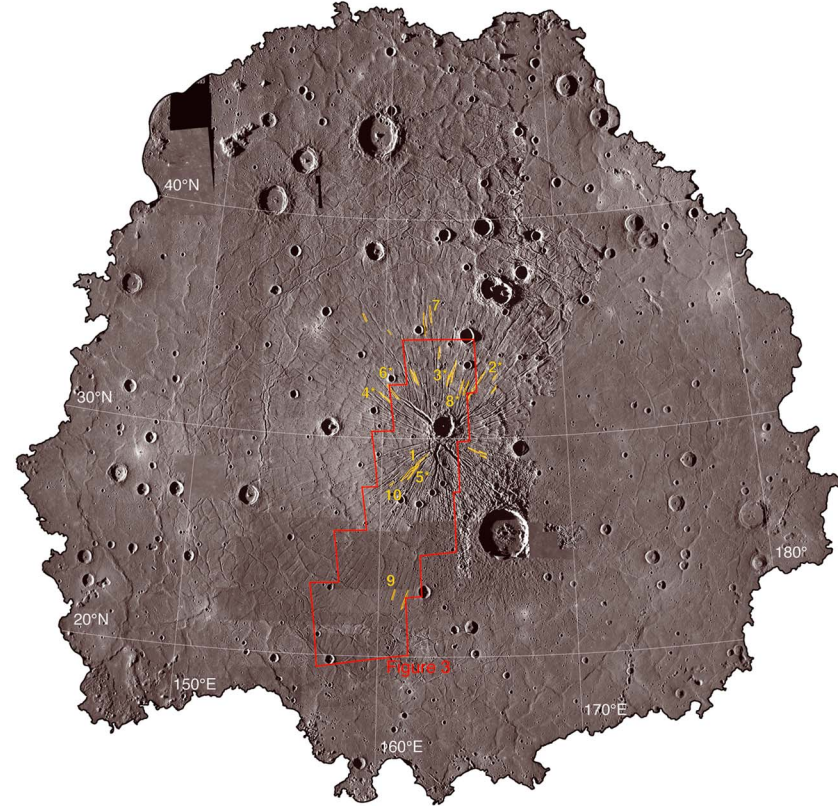


**Figure 2.** MDIS monochrome base map of the Caloris basin interior (250 m/pixel). Note the prominent basin-radial graben (Pantheon Fossae) in the center of the basin, and the basin-circumferential graben farther from the center. Also, note the many thrust-fault-related landforms throughout Caloris. The graben used for the displacement analysis shown in Figure 4 are numbered and shown in yellow. The outline of Figure 3 is shown in red. This map is in orthographic projection centered at 30°N, 162°E.

## 2. Faults in the Caloris Basin

[7] Whereas brittle deformation exterior to the Caloris basin is evident mainly as individual lobate scarps and wrinkle ridges, arrays of such features, or wrinkle-ridge-ringed ghost craters that host graben without a preferred orientation [Klimczak et al., 2012; Watters et al., 2012], faulting within the basin is manifest as a complex and systematic pattern of crosscutting graben and wrinkle ridges [e.g., Byrne et al., 2013]. Both wrinkle ridges and graben occur in radial and circumferential orientations with respect to the basin center (Figure 2). Throughout the basin, wrinkle ridges have mostly circumferential orientations, whereas the graben toward the center are found to be exclusively radial (Figures 2 and 3). With improved lighting geometries from MESSENGER orbital imaging, radial graben are observed to be more numerous and continue beyond what was originally described and mapped for Pantheon Fossae [Head et al., 2009; Watters et al., 2009a; Klimczak et al., 2010], to radial distances of up to 500 km from the basin center. Beyond that point, these structures are less common, and circumferential graben and graben lacking a preferred orientation dominate (Figure 2). Ridges in the outer part of the Caloris basin are also circumferential or of no preferred orientation (Figure 2).

[8] The abundance of faults in the Caloris basin provides a basis for assessing the rock-mechanical and geometric properties of the volcanic plains unit in which they formed.

We focused our analysis on the description and characterization of selected graben of Pantheon Fossae. In particular, we studied individual graben-bounding faults by investigating the displacement (slip) distribution along the fault, and we statistically evaluated the full graben population by examining the scaling behavior of fault displacements with respect to their lengths. We used results from this analysis to derive information on the depth extent of faulting throughout the basin by extrapolation to other faults within this population.

### 2.1. Fault Restriction in the Central Caloris Basin

[9] Klimczak et al. [2010] inferred a nearly constant maximum depth of faulting of ~3 km for the faults that bound a substantial number of graben in the central Caloris basin, and they suggested that those faults may have been vertically confined to a mechanical or stratigraphic layer. Layering in a faulted geological medium can have a marked influence on the dimensions of faults and their growth and scaling behavior [Soliva et al., 2005]. Thus, layering in the Caloris basin should be resolvable from a careful characterization of the fault dimensions.

[10] Fault dimensions include the fault length ( $L$ ) in the along-strike direction, as well as the width or height ( $H$ ), measured in the downdip direction, and the average fault displacement ( $D$ ). Information from at least two of these

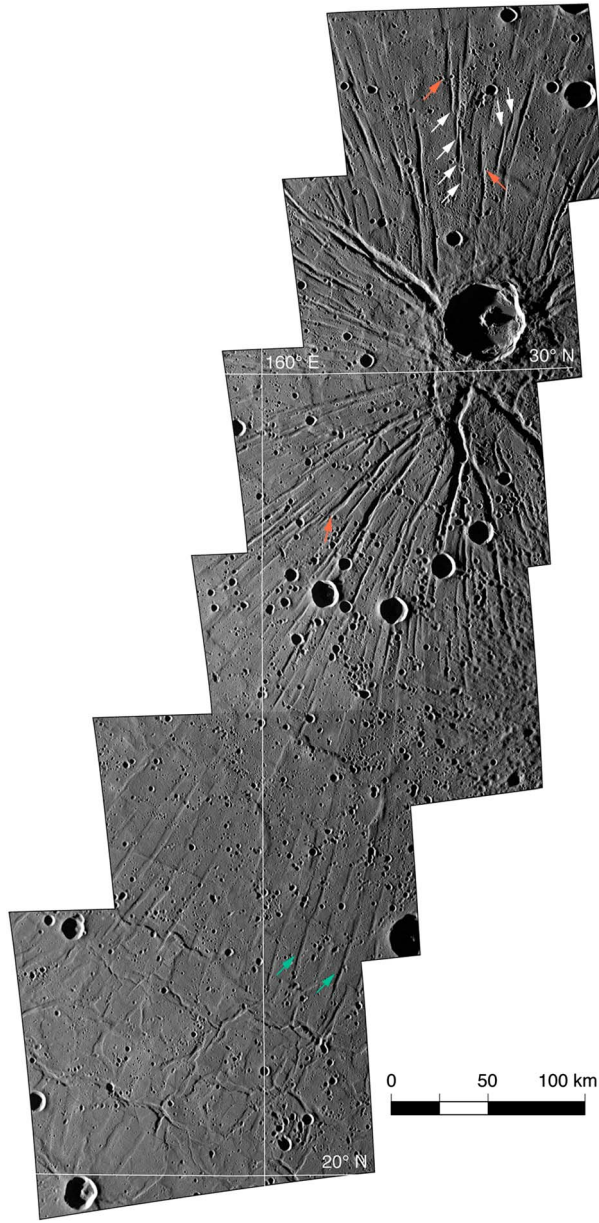


**Figure 3.** Mosaic of a set of MDIS wide-angle camera (WAC) images of the center of the Caloris basin, illustrating the structural complexity of the area. Note that none of the impact craters in this view is crosscut by any of the faults. Examples of isolated graben are indicated by green arrows, soft-linked graben (relay ramps) are indicated by white arrows, and hard-linked graben are marked with red arrows. This mosaic is in orthographic projection centered at 30°N, 162°E. Individual images used to assemble the mosaic include EW0220375075G, EW0220375107G, EW0220375141G, EW0220375183G, EW0220418418G, and EW0220418460G.

parameters can yield insight into the three-dimensional character of the fault surface, which is usually idealized as an ellipse [Irwin, 1962; Kassir and Sih, 1966; Willemse et al., 1996; Willemse, 1997; Schultz and Fossen, 2002] with an eccentricity defined as the aspect ratio of fault length to fault height ( $L/H$ ). In an infinite, elastic, homogenous medium, faults grow in a self-similar manner, i.e., they have a constant

fault aspect ratio [Schultz and Fossen, 2002]. The fault length is found to scale in proportion to the maximum displacement ( $D_{\max}$ ) [Cowie and Scholz, 1992a, 1992b; Scholz et al., 1993; Schultz and Fossen, 2002; Schultz et al., 2010] as:

$$D_{\max} = \gamma L, \quad (1)$$

where  $\gamma$  is a scaling coefficient related to rock-mechanical properties, the fault aspect ratio, and the driving stress conditions acting on the faults of a given population [Schultz and Fossen, 2002; Schultz et al., 2006]. Such fault growth behavior leads to a constant accumulation of displacement, with displacement minima at the fault tips and a maximum near the center of the fault, resulting in an overall peaked along-strike distribution of displacement [Cowie and Scholz, 1992b, 1992c; Dawers et al., 1993; Manighetti et al., 2001; Scholz, 2002].

[11] In contrast, vertical confinement of faults within a single stratum or mechanical layer limits fault growth and the further accumulation of displacement in the downdip direction. As a result, sufficiently large faults increase their lengths but not their heights [Soliva et al., 2005; Soliva and Benedicto, 2005; Soliva et al., 2006]. Such faults no longer grow in a self-similar manner, i.e., fault aspect ratios and thus eccentricities of the elliptical fault shape increase continuously as faults lengthen. This behavior results in a nonlinear displacement-to-length scaling relationship [Schultz and Fossen, 2002; Soliva et al., 2005; Soliva and Benedicto, 2005; Soliva et al., 2006; Polit et al., 2009], and a flat-topped (i.e., plateau-shaped) along-strike displacement distribution [Dawers et al., 1993; Manighetti et al., 2001; Soliva et al., 2005; Soliva and Benedicto, 2005; Soliva et al., 2006; Polit et al., 2009]. Although nonlinear displacement-to-length scaling and plateau-shaped displacement distributions can also arise from fault interaction and linkage [e.g., Cartwright et al., 1995; Wyrick et al., 2011], such fault growth behavior has been widely documented for restricted faults in a variety of terrestrial and planetary settings [Dawers et al., 1993; Soliva et al., 2005; Polit et al., 2009].

### 2.1.1. Displacement Distributions

[12] We measured the lengths and displacements of 31 faults in the Caloris basin (Figure 2) and constructed displacement distribution profiles for each. Fault lengths of single faults were measured from their mapped linear traces between the two fault tips identified on MDIS images. Displacements on surface-breaking normal faults on airless planetary bodies with minimal erosion can be obtained by measuring the relief of the trough-forming graben, which yields the vertical component of the fault displacement (the fault throw). However, neither stereophotogrammetry-derived topographic data sets nor laser altimetric data for Mercury are suited for such fine-scale topographic analysis, as those data sets do not have sufficient vertical or horizontal resolution, respectively. Therefore, fault throws were acquired by shadow measurements of graben on MDIS monochrome images with resolutions of 98–133 m per pixel; we measured shadow widths in 1 km increments along the entire length of the studied faults to obtain the throw distribution of each. For this analysis, we selected only the best illuminated and best preserved faults, as sufficiently accurate measurements could be made only for a limited range of lighting

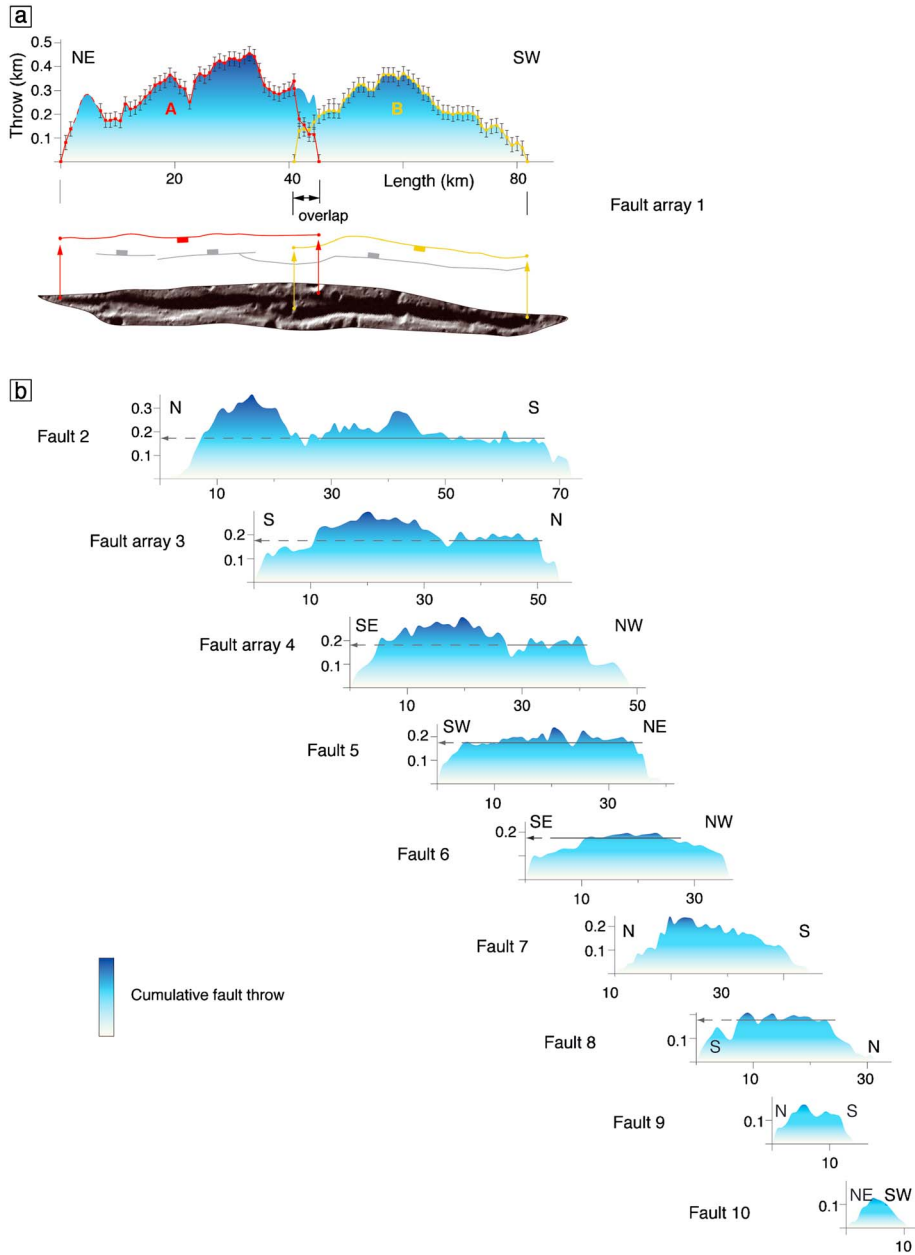


**Figure 4.** Measured distribution of fault throw along the length of several normal faults or fault arrays within the Caloris basin. Vertical exaggeration is 40:1. (a) Throw distribution along two overlapping faults shown in relation to an interpreted sketch map and an MDIS monochrome image. Each data point in the distribution represents one shadow measurement, and error bars denote the measurement uncertainty of  $\pm$  one pixel. The area in blue represents the distribution of the cumulative throw of the two individual faults. The skew of the maxima in displacement away from the centers of the individual faults and toward the center of the fault array indicates that the two fault segments interacted. (b) A series of throw distributions, shown at the same scale and arranged by decreasing fault length, indicate the dependence of fault throw on fault length. Longer faults have higher throws. Also, note that longer faults have plateau-shaped (i.e., flat-topped) distributions.

conditions and only for those faults for which the morphology was not later modified by impact cratering or mass wasting. Shadows were measured by pixel counting. Errors on the order of half a pixel ( $\sim 50\text{--}65$  m) are equivalent to measurement uncertainties of  $\pm 10$  m in the vertical direction. MLA profiles, where available, compare well to shadow measurements. (See Appendix A for a more

detailed description of the measurement procedure and assessment of sources of error.)

[13] A representative set of fault throw profiles, sorted by fault length, is shown in Figure 4, and a high-resolution view of these faults can be found in the supporting information. Profiles include fault throw data from arrays of two faults (Figure 4, fault arrays 1, 3, 4) as well as from individual faults

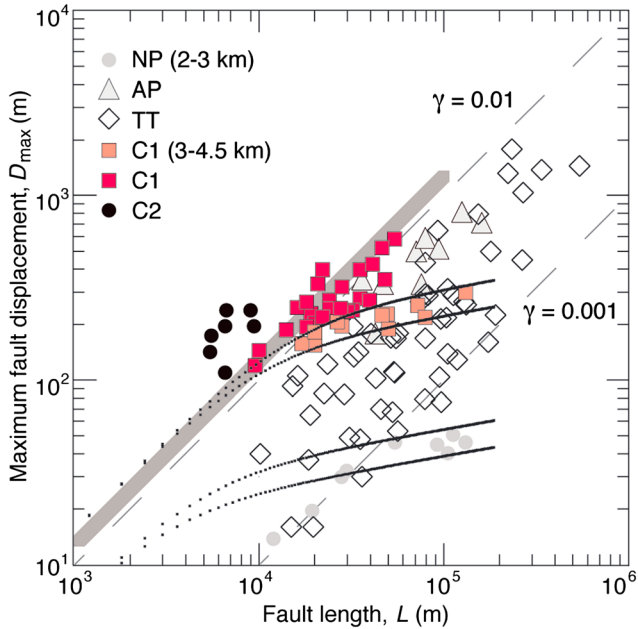


**Figure 5.** Maximum displacements of several planetary normal fault populations as functions of fault length. Note that shorter faults in the individual populations display a linear scaling behavior, whereas longer faults in some populations (i.e., those with a flat-topped distribution of fault throw) deviate from linear scaling, indicating fault restriction. The faults of Pantheon Fossae show both types of scaling behavior. Restriction curves (black dotted lines) are modeled according to the methodology described in Appendix B. The gray-shaded linear trend is the modeled best fit for the unrestricted faults of Pantheon Fossae. This best fit is for a semi-elliptical fault length ratio of  $0.5L/H=2$ . NP = northern plains graben, Mars, restricted to faults with heights of 2–3 km [Polit et al., 2009]; AP = Alba Patera, Mars, unrestricted [Polit et al., 2009]; TT = Tempe Terra, Mars, unrestricted [Polit et al., 2009]; C1 (this study) = Pantheon Fossae faults, Mercury, restricted to faults with heights of 3–4.5 km (light red) or unrestricted (red); C2 = faults with no preferred orientation in Caloris, no restriction apparent [Watters and Nimmo, 2010].

(Figure 4b, faults 2, 5–10). Individual graben consist of isolated fault pairs that show no evidence on MDIS images for interaction with other graben (Figure 3, green arrows). Arrays consist of sets of two or more graben in a closely spaced, en echelon geometry (Figure 3, white arrows). There is evidence for fault interaction within some of these graben arrays. Knowledge of whether faults interacted with each other or linked up is important for interpreting their scaling behavior and displacement distributions, a topic discussed further in section 2.1.3.

[14] Fault array 1 (Figure 4a), an example of a segmented graben structure in central Caloris, shows the fault throw distributions of two individual fault segments that overlap each other by ~5 km (errors in endpoint locations are  $\pm 30$  m). The fault array is >80 km long and has a maximum throw of ~500 m. The two segments of this array show peaked profiles, with their individual throw minima at the fault tips and maxima offset from the segment center toward the midpoint of the whole array, adjacent to the stepover between the

segments. Profiles with such a throw distribution resemble those for normal fault arrays on Earth [Peacock and Sanderson, 1994; Cartwright et al., 1995; Dawers and Anders, 1995; Willemse et al., 1996; Willense, 1997; Manighetti et al., 2001; Soliva and Benedicto, 2004; Soliva et al., 2008] and Mars [Polit et al., 2009] and indicate interaction between the individual fault segments.

[15] Fault 2 (Figure 4b) is a single, isolated 75-km-long fault with a generally plateau-shaped throw distribution, but with higher throws present in portions of the profile (at ~15 km and ~40 km along strike). Fault arrays 3 and 4 each consist of two individual segments and have total lengths of ~50 km. Although the arrays are in different parts of the Caloris basin (Figure 2), the two profiles look similar to one another and have throw distributions with plateaus along the segment closer to the basin center in each case. Because throw maxima are not located adjacent to the stepover region, individual fault segments likely have not interacted markedly. Isolated faults 5, 6, and 8 are ~30–40 km long, and all have generally flat-topped throw distributions (Figure 4b). Isolated faults 7, 9, and 10 show peaks in their throw distribution (Figure 4b).

[16] Throw distribution profiles for faults 2–10 (Figure 4b) highlight the scale dependence of fault displacement accumulation. Small faults, with lengths shorter than ~30 km, have peaked profiles indicative of self-similar, unrestricted fault growth. Many of the larger faults in the central Caloris basin, those for which lengths exceed ~30 km, in contrast, have flat-topped throw distribution profiles, indicating nonproportional fault growth (Figure 4b, faults 2–6, 8). We interpret such growth behavior as evidence for confinement of the longer faults to a distinct mechanical layer. The plateaus in the throw distributions for the longer faults therefore developed because these faults, once restricted, grew only in the horizontal direction, so they increased their lengths but did not grow further in the vertical dimension and thus did not accumulate additional downdip displacement. Plateaus in the throw distribution show local peaks (e.g., Figure 4b, fault 2), indicating that the fault surface grew to greater depth due to local variations in fault geometry or layer properties. Longer faults in the Caloris basin (those with lengths exceeding 30 km) that have peaked throw distributions had either unrestricted vertical growth, or penetrated into the underlying rock unit before resuming self-similar growth [Schultz and Fossen, 2002; Soliva et al., 2005; Soliva and Benedicto, 2005].

## 2.1.2. Displacement-Length Relations

[17] Comparison of the maximum displacements and corresponding lengths of faults within the same population gives insight into the scaling statistics and growth behavior of individual faults in that population. Downdip fault displacements can be obtained from fault throws for an assumed dip angle of the fault surface. For a dip angle of  $60^\circ$ , a value consistent with the optimum dip angle of normal faults in cohesive volcanic material [e.g., Jaeger et al., 2007], the approximate displacements of the faults can be calculated.

[18] There is a wealth of literature discussing the scaling relationships of fault displacements to fault lengths [Cailleux, 1958; Elliott, 1976; Watterson, 1986; Walsh and Watterson, 1988; Gillespie et al., 1992; Cowie and Scholz, 1992b; Dawers et al., 1993; Schlische et al., 1996; Schultz et al., 2008]. More recent studies have reached a general consensus on direct proportionality, i.e., a linear correlation between the two parameters [equation (1)] [Cowie and Scholz, 1992b; Dawers et al.,

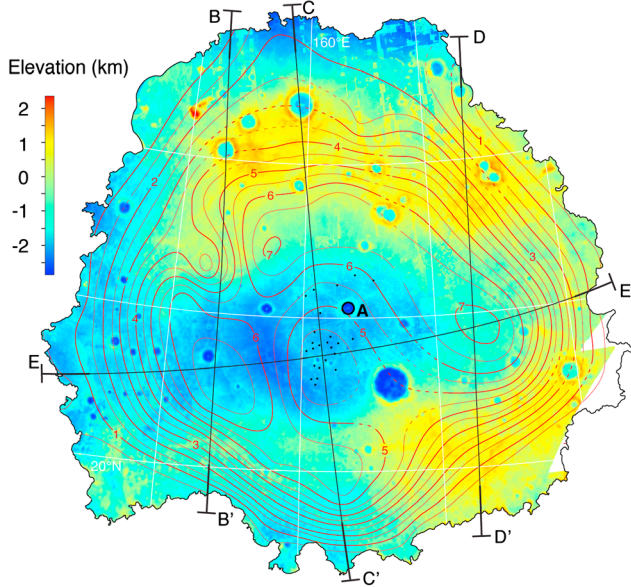


**Figure 6.** Contours of maximum depth extent of faulting for radial graben of Pantheon Fossae in relation to the topography of the Caloris basin. These maximum faulting depths can be interpreted as the minimum thickness of the mechanical unit in which the faults grew. Restricted faults are shown as black dots. Note the shoaling of the maximum depth extent of faulting in the central portions of the basin, near the topographic low to the southwest of Apollodorus crater (A), where an increased density of restricted faults is observed. The locations of the profiles (along segments of great circles) shown in Figure 7 are indicated by black lines. This map is in orthographic projection centered at 30°N, 162°E.

1993; Schlische *et al.*, 1996; Scholz, 2002; Schultz *et al.*, 2008]. In contrast, nonlinear scaling of fault growth is found to be representative of situations in which the fault is confined to a layer with rock-mechanical properties distinct from those of the underlying material [Schultz and Fossen, 2002; Soliva *et al.*, 2005; Schultz *et al.*, 2010]. Detailed field measurements confirm such scaling behavior in fault populations that are confined to a single mechanical layer [Soliva *et al.*, 2005; Soliva and Benedicto, 2005; Soliva *et al.*, 2006].

[19] Displacement maxima for 36 faults within Pantheon Fossae (Figure 2) are presented as a function of fault length in Figure 5, together with normal fault populations from Mars [Polit *et al.*, 2009] and elsewhere on Mercury (faults near the rim of the Caloris basin studied with Mariner 10 data by Watters and Nimmo [2010], data set C2). Whereas data sets from both Tempe Terra (TT) and Alba Patera (AP) on Mars show a largely linear  $D_{\max}/L$  scaling, a data set from the northern plains of Mars (NP) shows a systematic decrease in the slope of the  $D_{\max}/L$  relation with increasing  $L$  [Polit *et al.*, 2009]. This scaling behavior was interpreted [Polit *et al.*, 2009] as indicating confinement of faults to a layer 2–3 km thick (Figure 5).

[20] The data set we compiled from Pantheon Fossae shows both a linear relationship and a deviation from linear scaling (Figure 5, data set C1). Faults that follow the nonlinear (i.e., restricted) scaling (C1, light red squares) are located mainly in the central portion of Caloris basin, whereas faults that scale

linearly are found farther from the center (C1, red squares). This pattern indicates that only faults in the center of the basin are confined to a mechanical layer, whereas normal faults at greater radial distances from the center grew in an unrestricted, self-similar manner. The presence of restricted and unrestricted faults in different parts of the basin may be a function of variations in thickness and/or properties of the surficial mechanical layer across the basin.

[21] Displacement-versus-length data for graben in the Caloris basin with circumferential orientations or with no preferred orientation were derived by Watters and Nimmo [2010] from Mariner 10 images and stereo-derived topography. That data set (C2 in Figure 5), for which individual measurements have uncertainties of  $\pm 10$  m, is more or less consistent with our measurements but gives a slightly higher scaling coefficient. Differences in the scaling factor may arise from any of a variety of reasons, including fault populations with different length/height aspect ratios, different driving stress conditions, or measurement uncertainties.

[22] The values of the  $D_{\max}/L$  ratio of restricted faults can be converted to an estimate of the mechanical thickness of the layer in which they are restricted. Following the mathematical framework for three-dimensional fault scaling of Schultz and Fossen [2002], we varied parameters pertaining to the elliptical fault shape, host-rock properties, and stress conditions around the fault tip so as to achieve acceptable fits of the resultant analytical solution to our  $D_{\max}/L$  measurements. Details of the procedure are outlined in Appendix B. Our results indicate that fits to our  $D_{\max}/L$  measurements can be achieved only for a narrow range of input parameters. In particular, for a rock unit of mechanical properties consistent with dry basalt, together with shear stress conditions appropriate for such materials on Mercury, the faults that deviate from linear scaling are restricted to fault heights of 3–4.5 km (Figure 5). For a 60° fault dip angle, this restriction corresponds to a vertical confinement of the faults within a mechanical unit of ~2.6–4 km thickness.

### 2.1.3. Fault-Linkage Effects

[23] Fault linkage occurs when the overlap and spacing between two or more faults are sufficiently close that the faults mutually influence each other's growth. In map view, the linkage of normal faults is evident by ramps in the stepover region (relay structures) or by abrupt bends (jogs) in the fault trace. In some cases, fault linkage can have effects on the  $D_{\max}/L$  relationship and slip distribution profiles that are similar to those produced by fault confinement to a mechanical or stratigraphic layer. An array of several small, softly linked faults, i.e., interacting but not fully coalesced fault segments [see Schultz, 2000] with substantial overlap, might show flat-topped (i.e., plateau-shaped) slip distributions, and a population of linked faults can show a nonlinear  $D_{\max}/L$  scaling relationship [e.g., Cartwright *et al.*, 1995; Schultz *et al.*, 2010; Wytrick *et al.*, 2011] resembling that of restricted faults. Although linked faults are present in the Caloris smooth plains (e.g., Figure 4a), fault throw distributions (Figure 4b) generally show profiles typical of either restricted or unrestricted fault growth [e.g., Manighetti *et al.*, 2001], and all flat-topped throw distribution profiles show plateaus at around the same maximum displacement value of ~180 m (Figure 4b). These combined results indicate that fault linkage has at most a minor influence on our analysis of fault scaling.

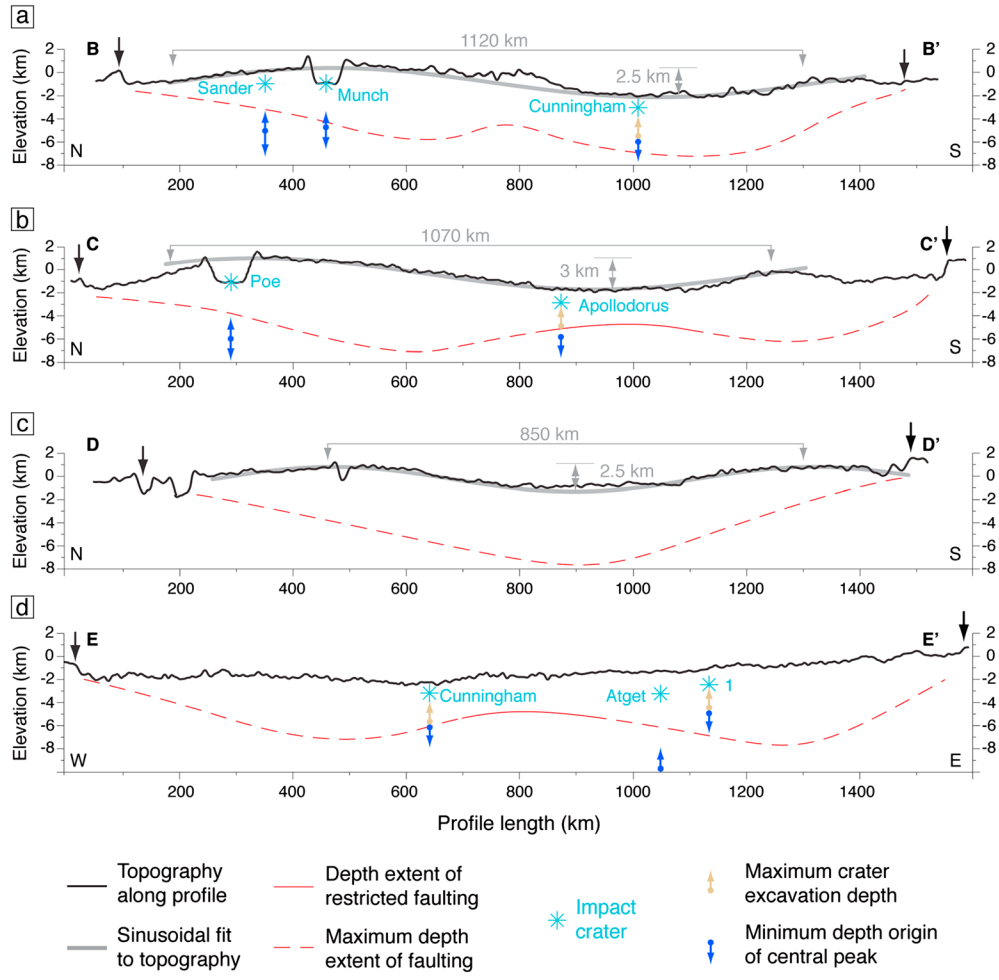


**Figure 7.** Topographic profiles through the Caloris basin, together with inferred mechanical stratigraphy (the red line shows the maximum depth of faulting; the line is solid where faults are restricted and dashed where faults are unrestricted). The location of the basin rim along each profile is indicated by a black arrow. Also shown with arrows are maximum excavation depths (upward arrow) and minimum depths of origin of central peak material (downward arrow) for large impact craters [Ernst et al., 2010]. Arrows are blue for craters that excavated material spectrally distinct from the surrounding terrain and tan for craters that excavated material spectrally similar to the surface unit. If a nearby crater does not fall directly on the profile, its elevation is projected onto the profile and thus might differ from the topography shown. All profiles are shown with 20:1 vertical exaggeration. (a) Profile B–B' shows sinusoidal topography of 1120 km wavelength and 2.5 km amplitude. Inferred mechanical stratigraphy shows notable undulations in the depth to the base of the surface mechanical unit; the undulations are generally consistent with spectra of material excavated by large craters and the inferred excavation depths. (b) Profile C–C' shows sinusoidal topography of 1070 km wavelength and 3 km amplitude. Inferred mechanical stratigraphy shows shoaling toward the basin center, consistent with spectra of crater ejecta and inferred excavation depths. (c) Profile D–D' shows sinusoidal topography of 850 km wavelength and 2.5 km amplitude. Inferred mechanical stratigraphy shows steady thickening toward the center of the profile. (d) Profile E–E' shows minor topographic undulations, but they cannot be modeled with simple sinusoidal functions. Inferred mechanical stratigraphy shows shoaling toward the basin center, consistent with spectra of crater ejecta and inferred excavation depths.

## 2.2. Depth Extent of Faulting

[24] The established statistical relationship between maximum displacement and fault length for the structures in Pantheon Fossae (Figure 5) can be used to obtain information on fault height and thus the depth extent of faulting for every fault in this population. Where fault growth is restricted, the fault height can be directly related to the depth of a mechanical boundary. Where faults grew in an unrestricted manner,

however, information on fault height can be used only to infer the maximum depth extent of faulting. This value can then be used to infer the minimum depth extent of the unit in which the faults grew.

[25] The three-dimensional fault scaling analysis yielded good fits for unrestricted faults with constant length aspect ratios of  $0.5L/H=2$  (see Appendix B for details), such that the length of the fault is approximately four times the fault

height. From this relationship, and for a  $60^\circ$  fault dip angle, the depth extent of faulting can be estimated for every radial fault in the basin. We estimated the depth of faulting of  $\sim 150$  faults with mostly basin-radial orientations throughout Caloris (see the supporting information).

[26] From the data set for maximum depth of faulting below the topographic surface in the Caloris basin, we interpolated with the “blockmean” and “surface” tools in the open geo-processing software GMT [Wessel and Smith, 1998] (<http://gmt.soest.hawaii.edu/>). From this interpolation, we obtained a contour map that approximates the maximum depth of faulting below the present topography (Figure 6). The contours, shown in relation to the basin topography [Preusker et al., 2011], illustrate that the maximum depth extent of faulting is variable across the basin, with graben-bounding faults penetrating from  $\sim 4$  to more than 7 km below the surface. A zone in which the maximum faulting depth is  $< 4.5$  km, within which faults are inferred to be confined to a mechanical unit on the basis of their displacement/length relationships, is located near the basin center. That zone is surrounded by an annulus in which faults penetrate to somewhat greater depths (Figure 6). The maximum depth extent of faulting lessens toward the basin rim.

[27] From displacement distributions and the analysis of maximum displacement versus fault length, we infer that the majority of faults are confined to a mechanical unit near the center of Caloris basin, but we find no evidence for confinement outside of the central basin zone. These observations suggest that many of the graben we have analyzed are contained within a single coherent mechanical unit. Under this interpretation, the thickness of this unit correlates directly with the maximum depth extent of faulting in regions of fault confinement, whereas only minimum estimates of the thickness of the mechanical unit may be deduced in regions of unconfined fault growth. Contours of maximum extent of faulting (Figure 6) may be interpreted, by this view, as isopachs that represent the minimum thickness of the uppermost mechanical layer in the Caloris basin, and so imply a mechanical boundary at those depth values or greater depths. Alternatively, regions of greater maximum depths of faulting may correspond to areas in which faults penetrated a mechanical boundary and propagated into the underlying unit.

[28] The systematic decrease of fault width and length toward the edge of the basin for graben with no preferred orientation to the basin rim (see supporting information) is suggestive of a decreased penetration depth of the faults. By a similar argument, the presence of a wider, younger set of graben in the central Caloris basin with larger geometric proportions for the individual structures (Figures 2 and 3) has been regarded as indicative of a greater depth extent of faulting for these faults than the adjacent, narrower structures [Klimczak et al., 2010]. However, these wider graben are no longer fully preserved because subsequent impacts have modified portions of them, and so detailed information on their lengths, slip distributions, and scaling behavior is unreliable for any interpretation of the stratigraphy of the rocks beneath the uppermost mechanical layer of smooth plains. Notwithstanding such limitations, these graben display widths of up to  $\sim 9$  km and so they must have penetrated the mechanical boundary inferred to be present at  $\sim 4$  km depth in the center of Caloris basin.

### 3. Topographic Undulations in and Around the Caloris Basin

[29] The topography of the Caloris basin (Figures 1 and 6) is characterized by long-wavelength undulations of the basin floor, with some areas having been vertically displaced so as to be now above the basin rim [Zuber et al., 2012]. In addition, the flat portions of floors of several impact craters within Caloris are tilted in the same direction as the downslope trend of the long-wavelength topography [Balcerski et al., 2012, 2013; Zuber et al., 2012]. Similar relationships between long-wavelength topography and tilted craters can be observed in the regions exterior to the basin (Figure 1).

[30] The undulations can be described as gentle, elongate topographic highs and lows, and systematic trends of crater floor tilts support the mapping of long-wavelength troughs and crests (Figure 1). Within the Caloris basin, there is a trough in the basin center and two crests to the north and south of that central topographic low (Figure 1). In the region west of the basin, a crest can be mapped through the topographic high that hosts Raditladi basin, as well as two associated troughs to its north and south (Figure 1).

[31] In cross-strike profiles, the topographic undulations can be approximated by long-wavelength (850–1300 km) but low-amplitude (2.5–3 km) harmonic functions (Figures 1c and 7). Profile A–A' (Figure 1c) shows undulations outside the Caloris basin that match a sinusoidal form with a wavelength of 1300 km and an amplitude of 3 km. Profiles B–B' to E–E' (Figure 7) show that topographic trends within the Caloris basin match sinusoidal forms of somewhat shorter wavelengths (850 to 1120 km) than but similar amplitudes (2.5 to 3 km) to those for undulations outside the basin. The axes of all mapped troughs and crests in and around the Caloris basin are preferentially oriented approximately east–west (Figure 1), but the east–west cross section E–E' (Figure 7d) shows that some minor topographic variations also occur perpendicular to the orientation of the major axes of the undulations.

[32] The presence of topographic undulations inside the faulted and mechanically stratified Caloris basin is useful for gaining insight into the nature of topographic changes on Mercury. Combining topographic information with estimates of mechanical layering at depth allows us to interpret the subsurface structure of the basin and permits assessment of the processes involved in long-wavelength deformation on Mercury. This assessment provides information on lithologic stratigraphy and rock-mechanical properties of the smooth plains, the origin of the long-wavelength topographic undulations, and the timing of topographic changes relative to smooth plains emplacement, smooth plains deformation, and the cratering record within the Caloris basin.

## 4. Discussion

### 4.1. Depth Extent of Faulting Versus Mechanical/Lithologic Stratigraphy

[33] Correlation of the depth extent of faulting with topography for four representative profiles across the Caloris basin shows that faults grew to different depths below the present surface (Figure 7). The depth extent of faulting in the Caloris basin appears to correlate with long-wavelength topography in some locations (e.g., Figure 7c) and to anticorrelate with long-wavelength topography in other

locations (e.g., Figure 7b). Under our interpretation that the maximum depth of faulting represents the minimum thickness of the uppermost mechanical layer, such relations indicate variable but systematic thickness changes in the mechanical stratigraphy of Caloris. For the alternative scenario, under which the unrestricted graben-bounding faults penetrated the bottom of the upper mechanical layer, a layer boundary would be discernable only in the center of the basin, where faults are restricted.

[34] Profile B–B' (Figure 7a) in the western part of the Caloris basin (Figure 6) shows a topographic high (crest) to the north and a low (trough) to the south. The depth extent of the faults generally increases inward from the basin margin but appears to shoal somewhat beneath the basin center. The depth extent of faulting appears to anticorrelate with the long-wavelength topography along profile C–C' through the center of the basin (Figure 7b); i.e., unrestricted faults penetrate deeper beneath high-standing terrain and fault restriction indicative of a mechanical contrast occurs beneath long-wavelength lows near the basin center. Profile D–D' through the eastern portion of the basin shows a steady increase of the depth extent of unrestricted faulting toward the center (Figure 7c). The east–west–oriented profile E–E' (Figure 7d) shows fault restriction near the center of the Caloris basin and unrestricted faults that penetrate deeper away from the center.

[35] Many large impact craters are found on the smooth plains within the Caloris basin (Figure 2). Several of the larger impact craters have exposed spectrally distinct materials in their ejecta or on their floors and central peaks [e.g., Ernst et al., 2010]. Spectral variations among the major color units on Mercury are generally attributed to compositional differences [Robinson et al., 2008; Blewett et al., 2009]. Different spectral properties of material exposed in the ejecta or central peaks of impact craters may therefore yield additional information on the lithological stratigraphy within Caloris. Ernst et al. [2010] estimated the depth of excavation of spectrally distinct materials associated with large craters in the central Caloris basin. These authors concluded, on the basis of the diameters of several craters that expose spectrally distinct materials on their central peaks but not on their floors or ejecta, that the high-reflectance red plains that partially fill the central Caloris basin must generally be between 2.5 and 4 km thick. This range is remarkably similar to that for the depth of confinement of fault growth (Figure 5) in the central portion of the basin (i.e., 2.6–4 km).

[36] We have compared estimates of the depth of excavation of spectrally distinct material by several impact craters within the Caloris basin (on the basis of the results of Ernst et al. [2010] and shown in the supporting information) with the mechanical stratigraphy inferred from the fault analysis of this study along the topographic profiles in Figure 7. Estimates can be made for the maximum depth of excavation of materials in the ejecta and crater floor as well as for the minimum depth of origin of the central peak (see Ernst et al. [2010] and references therein). Profile B–B' (Figure 7a) incorporates depth information from three large craters: Sander, Munch, and Cunningham. Sander and Munch craters (with diameters of 47 and 57 km, respectively) show material spectrally distinct from surrounding terrain in their ejecta, floor, and central peaks, so a stratigraphic boundary must overlie the maximum excavation depth. This finding

is consistent with stratigraphic relationships inferred from the depth extent of faulting. Cunningham crater (38 km in diameter), in contrast, exposes spectrally distinct material only on its central peak, constraining the change in lithology to a depth between the excavation depth of the ejecta and that of the central peak. The estimated minimum excavation depth of the spectrally distinct central peak material of Cunningham is somewhat less than the inferred depth of the mechanical boundary in the vicinity of the crater, but as this value is a minimum this observation is not inconsistent with our findings.

[37] Along profile C–C' (Figure 7b), the depths of excavation of Poe and Apollodorus craters both show a good correlation to the inferred mechanical stratigraphy. Poe crater (77 km in diameter) displays spectrally distinct material in its ejecta and its central peak, and both associated estimates of excavation depth exceed the depth of the inferred mechanical boundary. Apollodorus crater (41 km in diameter), in contrast, displays spectrally distinct material only on its central peak. The estimated minimum excavation depth of central peak material for Apollodorus exceeds the inferred depth of the mechanical boundary, which in this area is given by the depth of confinement of the graben-bounding faults. Along profile E–E' (Figure 7d), the depths of excavation of Cunningham, Atget, and an unnamed crater (marked as “1”) also correlate with mechanical stratigraphy. For Cunningham crater, as for Apollodorus along profile C–C', only the minimum depth of excavation of central peak material exceeds the inferred depth of the mechanical boundary, showing a good fit between changes in lithology and mechanical properties inferred from faulting depths. Atget crater (100 km in diameter), in contrast, exposes spectrally distinct material on its floor as well as its central peak, and the estimated depths of excavation for material in both parts of the crater exceed the inferred depth of the mechanical boundary. The unnamed crater (31 km in diameter) shows very little spectrally distinct material on its central peak. Its estimated minimum depth of excavation of central peak material is somewhat shallower than the inferred mechanical boundary, but because portions of the central peak are not spectrally distinct from the ejecta and surrounding terrain for this crater, and because its excavation depth estimate is a minimum, these results do not conflict with our findings.

[38] The broad agreement between the excavation depths of spectrally distinct material and the depth of the mechanical boundary beneath the Caloris basin interior inferred from the maximum depth extent of faulting suggests that the change in spectral properties at depth beneath the interior smooth plains coincides with the base of the upper mechanical layer. Moreover, results of our three-dimensional fault scaling analysis suggest that the graben formed in a mechanically strong, dry basaltic rock mass (see Appendix B for details). These physical rock properties are consistent with geochemical data obtained by MESSENGER's X-Ray Spectrometer (XRS), which, on the basis of elemental surface abundances, indicate a basalt-like composition for the smooth plains within the Caloris basin interior [Weider et al., 2012]. The consistency between mechanical, spectral, and geochemical properties for these plains suggests that the mechanical unit in which the graben formed relates lithologically to a ~4-km-thick smooth plains layer of basaltic composition that is compositionally distinct from the underlying material.

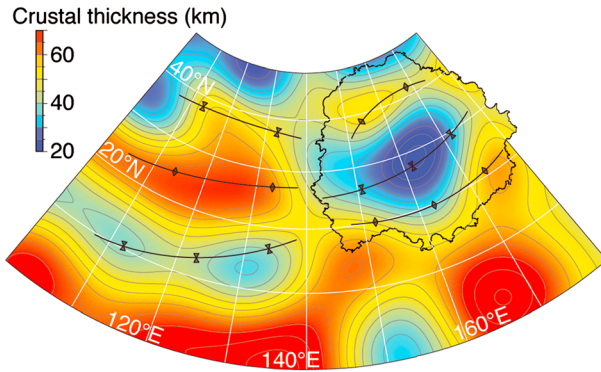


**Figure 8.** Variations in crustal thickness [Smith *et al.*, 2012] in and around the Caloris basin (black outline). The area shown corresponds to that in Figure 1a, and the positions of axes of topographic crests and troughs correspond to those in Figure 1b. Note the tendency for axes of crests and troughs to coincide with zones of thicker and thinner crust, respectively. This map is in north polar stereographic projection centered at 140°E.

#### 4.2. Tectonic Evolution of the Caloris Basin and Global-Scale Implications

[39] The crosscutting and superposition relationships among faults, impact craters, and topography allow a reconstruction of the relative timing of the events that led to the present morphological and topographic characteristics of the Caloris basin. The infill consisted at least of an upper smooth plains unit that is ~4 km thick and is compositionally different from underlying units. The lack of evident impact craters partially or fully buried by interior smooth plains material indicates either that any younger craters on the Caloris basin floor were deeply buried or that plains emplacement followed basin formation so closely that there was insufficient time for large impact craters to form.

[40] After their emplacement, the Caloris smooth plains were widely deformed by extensional and contractional tectonic structures, and a multitude of impact craters were superposed on the plains (Figure 2). No fault-related landforms, either graben or wrinkle ridges, appear to crosscut any of the impact craters (Figure 3). This result indicates that the majority of both extensional and contractional faulting occurred within the relatively short time span between plains emplacement and the formation of the earliest of the large impact craters visible today. That the flat portions of the floors of many of the larger craters in the Caloris basin are tilted [Balcerski *et al.*, 2012; Zuber *et al.*, 2012] (Figure 1) shows that the process that produced the topographic changes was active after the formation of the brittle deformational features and at least some of the subsequent cratering of the Caloris interior plains.

[41] Long-wavelength topographic changes can be detected globally on Mercury, as there is evidence for such changes both outside the Caloris basin (Figure 1) and elsewhere on the planet [Klimczak *et al.*, 2012; Solomon *et al.*, 2012; Zuber *et al.*, 2012]. Comparison between the different regions that were affected by topographic changes and their stratigraphic relationships to volcanic plains units, faults, and craters may provide insights into the timing and duration of the process that led to these changes. For example, a topographic

rise [e.g., Zuber *et al.*, 2012] located near the center of the northern volcanic plains hosts ghost craters that all tilt away from the crest of the rise, whereas many of the fresher craters there have horizontal crater floors [Klimczak *et al.*, 2012]. This pattern indicates that there, too, the process responsible for the topographic changes was active after plains emplacement. For both the northern and Caloris interior plains, Balcerski *et al.* [2013] categorized the tilted craters that superpose the plains by state of degradation and found that changes in topography occurred relatively recently in Mercury's geologic history. Information on the start and duration of changes in long-wavelength topography is more challenging to obtain, however, and requires detailed characterization of crater ages in relation to measured floor tilts.

[42] Prior to the availability of global topographic data sets, long-wavelength topographic undulations were predicted to be present on Mercury as lithospheric folds [Hauck *et al.*, 2004; Dombard and Hauck, 2008]. Such folds were suggested to have been one manifestation of the radial contraction of Mercury as its interior cooled, because estimates of global contractional strain and radius change derived from the estimated horizontal shortening accommodated by the thrust faults that underlie lobate scarps [Strom *et al.*, 1975; Watters *et al.*, 1998, 2009b; Watters and Nimmo, 2010] were far lower than predictions from thermal history models [Hauck *et al.*, 2004; Dombard and Hauck, 2008].

[43] The horizontal contractional strain,  $\varepsilon$ , across the undulations on Mercury inferred from the observed wavelengths and amplitudes of the undulations, however, is on the order of  $10^{-5}$  or less. Strains of such low magnitude would contribute insignificantly to the average radial shortening from global contraction. Furthermore, numerical modeling of elastic folding generally suggests that buckling of a thick lithosphere is difficult to achieve under likely stress conditions [McAdoo and Sandwell, 1985; Turcotte and Schubert, 2002; Bland and McKinnon, 2012]. Nonetheless, numerical simulations have shown that buckling of a lithosphere with elastic-plastic [McAdoo and Sandwell, 1985] or visco-plastic [Zuber, 1987; Montési and Zuber, 2003] deformational behavior can occur without unrealistically high stress magnitudes.

[44] Topographic undulations could also result from uneven vertical loading of the top of the lithosphere. Indeed, the area in and around the Caloris basin was affected by extensive flood volcanism [e.g., Denevi *et al.*, 2013] and the emplacements of large volcanic loads inside and surrounding the basin. However, topographic undulations occur on a broader spatial scale than the volcanic units and have deformed to the same extent areas that have been volcanically buried and other locations that have not. Moreover, these undulations have wavelengths and amplitudes that are too nearly harmonic to reflect the irregular distribution of volcanic units [Denevi *et al.*, 2013] as sources of lithospheric loading. Therefore, we conclude that lithospheric loading is not likely to have been the dominant source of the topographic undulations.

[45] Long-wavelength topographic undulations might also be the result of dynamic topography produced by mantle convective processes. Numerical models show that mantle convection may have occurred on Mercury [King, 2008; Roberts and Barnouin, 2012; Michel *et al.*, 2013] despite a mantle thickness of less than 400 km [Smith *et al.*, 2012; Hauck *et al.*, 2013]. The axes of the crests and troughs of the topographic undulations (Figure 1b) show some

correlation with crustal thickness variations derived from a model of Mercury's gravity field expanded to spherical harmonic degree and order 20 [Smith *et al.*, 2012] (Figure 8). Axes of troughs largely coincide with thinner regions of the crust, whereas axes of crests mainly collocate with areas of thicker crust. Because the wavelengths of model artifacts for the current harmonic gravity field solution are on the order of those of the topographic undulations, however, confirmation of this finding and further geophysical interpretation will require solutions for Mercury's gravity field to substantially higher harmonic degree and order.

[46] The orientations of the graben and wrinkle ridges appear largely unrelated to the long-wavelength changes of topography within the basin. This lack of correlation is consistent both with the inference that the faults formed as products of basin-localized tectonics well before the topographic changes as well as with the low strains ( $\epsilon \sim 10^{-5}$ ) accommodated by the undulations. Although numerical results are supportive of the idea that faulting may have accompanied the formation of lithospheric-scale undulations [Neumann and Zuber, 1995; Montési and Zuber, 2003], we infer that stresses associated with the formation of the topographic undulations on Mercury were too small to have exerted a large effect on preexisting or younger brittle structures.

[47] The presence of topographic undulations on Mercury, and their stratigraphic relationship with other landforms in the Caloris basin, not only allows for better characterization of the geologic and tectonic evolution of the basin but also has implications for dynamic processes and the thermal evolution of the planet's interior. Global contraction or mantle convection as candidate processes for the topographic changes both suggest that the observed undulations may involve the entire lithosphere. If so, wavelengths and amplitudes of the undulations may hold useful information regarding the rheological properties of the crust and mantle during the time of their formation, as rheological contrasts have a major impact on the geometry of the undulations. For example, theory of large-scale buckling of a planetary lithosphere [Ricard and Froidevaux, 1986; Montési and Zuber, 2003] shows that its mechanical structure controls the wavelength of deformation [Montési and Zuber, 2003]. Moreover, if these long-wavelength undulations are indeed related to mantle dynamic processes that occurred late in Mercury's history, a timing suggested by the numerous tilted craters [Balcerski *et al.*, 2013], such a result would imply that convection cells of sizes comparable to the half-wavelength of the undulations characterized Mercury's interior on a similar timeframe.

## 5. Conclusions

[48] By means of a detailed fault displacement analysis, we have established the maximum depth extent of faulting for the Pantheon Fossae radial graben complex in the Caloris basin. Our results show that in the center of the basin, graben-bounding faults are likely confined to a mechanical layer, consistent with previous studies [Klimczak *et al.*, 2010]. Farther from the basin center, normal faults grew in an unconfined manner or penetrated the mechanical unit. Under the first of these interpretations, the maximum depth extent of faulting for this latter group of structures can be interpreted as representing the minimum thickness of the mechanical unit in which the faults grew. Estimates for the

depth of excavation of exposed materials in impact craters that show spectral differences from the surface plains unit [Ernst *et al.*, 2010] correlate well with our inferred mechanical stratigraphy, supporting the inference that changes in rock mechanical properties generally coincide with variations in rock spectral properties.

[49] Furthermore, characterization of the long-wavelength topography suggests that the area in and around the Caloris basin has been affected by topographic changes, with elongate high-standing and low-lying regions corresponding to the crests and troughs of sinusoidal forms when viewed in cross section (Figure 7). Several of the cross sections through the Caloris basin indicate that the thickness of the uppermost mechanical unit of the Caloris smooth plains varies systematically with topography, suggesting a complex subsurface structure of the basin.

[50] The stratigraphic and topographic properties of the Caloris plains, coupled with crosscutting and superposition relationships among plains, craters, and faults, yield insight into the relative timing of events in the basin. In particular, the processes responsible for the topographic changes were active well after both plains emplacement and most brittle deformation inside Caloris. The stratigraphic and temporal relationships of topographic undulations have global implications, as these features occur elsewhere on Mercury and thus may be the surface manifestations of such interior processes as global contraction or mantle convection.

## Appendix A: Error Assessment

[51] Shadows within graben were measured on individually processed MDIS images to maintain the highest possible resolution (~98–133 m per pixel). Measurements were taken from orthographic projections (centered on each studied graben structure to minimize parallax errors) by counting the pixels perpendicular to the trace of a graben-bounding fault. By accounting for solar incidence angle and graben orientation relative to solar azimuth, shadow measurements can be converted to the topographic difference between the crest of the graben and its floor (i.e., the fault throw). Optimal lighting conditions are for solar incidence angles of 60–80°; within this range, we found many graben for which shadows were sufficiently wide to be resolved across several pixels but were not so wide that the shadow covered the entire graben floor.

[52] The vertical distance between graben crest and floor, corresponding to the fault throw, was derived from trigonometric relationships between solar azimuth and incidence angles and the measured shadow width. Measurement uncertainties are on the subpixel scale. Errors in our shadow width measurements can be assumed to be on the order of half a pixel (i.e., approximately 50–65 m). This error reduces to an uncertainty of  $\pm 10$  m in the vertical direction, so each estimate of fault throw can be assumed to deviate by less than  $\sim 20$  m from the actual topographic difference between crests and floors of the graben. For example, a shadow width of  $1500 \pm 65$  m across a graben that is illuminated at a solar azimuth of 75° with a solar incidence angle of 80° yields a fault throw of  $220 \pm 14$  m. A strong correlation between our measurements and throws derived from MLA profiles across some of our measured graben (Figure A1) shows that throw estimates derived from shadow measurements are robust.

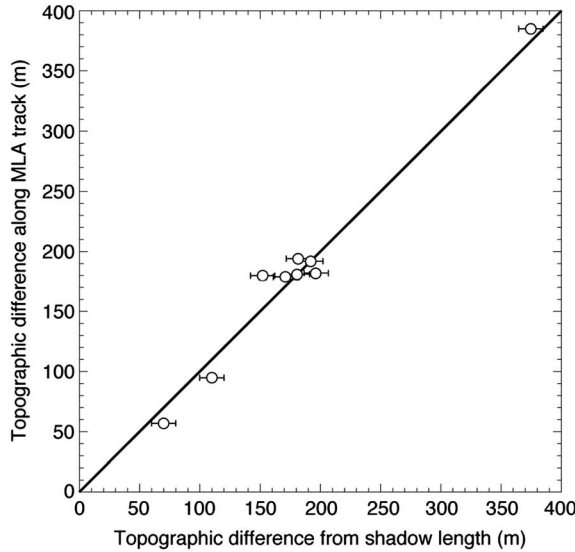


**Figure A1.** Fault throws estimated from shadow measurements compared with the throws obtained for the same faults from MLA profiles. Shadow measurements compare well with MLA data, indicating that any systematic errors in this analysis are small. The straight line has a slope of unity.

[53] Despite minimal erosion on Mercury, some sources of uncertainty exist for the interpretation of topographic offsets as actual fault throws, because cratering and mass wasting may have modified topography in places. Furthermore, the graben floors were assumed to be horizontal for the analysis, but asymmetric graben geometries and tilted graben floors would introduce some error in the throw estimates. Converting throw to displacement could introduce further uncertainty, as fault dip angles were assumed to be uniform at 60°. These uncertainties affect absolute fault displacements. Data trends, however, such as the shape of the distribution of fault throws, or the slope of a population of  $D_{\max}$  versus  $L$ , should be little affected, as most uncertainties are systematic and would affect all measurements more or less equally.

## Appendix B: Three-Dimensional Fault Scaling

[54] For a fault of horizontal length  $L=2a$  and downdip height  $H=2b$ , the three-dimensional scaling relationship for the shear strain accommodated on the elliptical fault surface can be further specified from equation (1) as:

$$\frac{D_{\max}}{L} = \gamma = \frac{2(1-v^2)}{E} \frac{\left\{ \sigma_d - \sigma_y \left[ 1 - \cos \left( \frac{\pi}{2} \frac{\sigma_d}{\sigma_y} \right) \right] \right\}}{\sqrt{\left( \cos^2 \theta + \left( \frac{b}{a} \right)^2 \sin^2 \theta \right)} \sqrt{1 + 1.464 \left( \frac{g}{b} \right)^{1.65}}}, \quad (A1)$$

where  $v$ ,  $E$ , and  $\sigma_y$  are the Poisson's ratio, Young's modulus, and yield strength at the fault tip, respectively, of the host rock [Schultz and Fossen, 2002; Schultz et al., 2006]. The parameter  $\sigma_d$  is the cumulative driving stress, accounting for the total number of slip events necessary to produce the observed fault lengths and displacements [Cowie and Scholz, 1992a; Scholz, 1997; Gupta and Scholz, 2000; Schultz,

2003]. The angle from the center of the fault plane to a point on its tip,  $\theta$  [Irwin, 1962; Kassir and Sih, 1966], is equal to zero when displacements are analyzed along the horizontal axis of the fault, i.e., its length, so that the term in equation (A1) that is a function of  $\theta$  reduces to unity.

[55] For crustal scales, values for Young's modulus of a fractured rock volume (rock mass) on a planetary surface are best approximated with the deformation modulus [Bieniawski, 1989; Schultz, 1996], and the modulus increases with depth [Rubin, 1990] as a function of the planetary gravitational acceleration and rock density [Schultz et al., 2006]. We assumed a dry basaltic rock mass of density  $\rho=3.1$  g/m<sup>3</sup>, yielding  $E=24$  GPa at and near the surface of Mercury, a value consistent with considerations by Schultz et al. [2006]. Lower densities result for less competent volcanic rock masses [Bieniawski, 1989], as recently confirmed for surface units on the Moon [Wieczorek et al., 2013], with values for the deformation modulus also lower. Values of the deformation modulus increase only slowly with depth on Mercury, due to the comparatively low surface gravitational acceleration. Poisson's ratio was assigned a typical value for rock of  $v=0.25$ . The unfaulted, dry, basaltic rock mass in the Caloris basin is expected to be mechanically strong, so values of  $\sigma_y$  were taken to be  $15\pm 5$  MPa, on the basis of estimates obtained with the Hoek-Brown failure law [Hoek and Brown, 1980; Schultz et al., 2006; Jaeger et al., 2007]. Values for the ratio of yield strengths to driving stresses are found to be approximately 2–3 [Cowie and Scholz, 1992a; Schultz and Fossen, 2002; Wilkins and Schultz, 2005].

[56] The parameters pertaining to rock properties and stress conditions are expected to remain generally constant throughout a given rock mass, so that the solution for equation (A1) depends mainly on the shape of the faults. Following Polit et al. [2009], the fault shape was parameterized by the fault aspect ratio, i.e., the ratio of fault length to fault height  $L/H$  for buried faults and by the ratio  $0.5L/H$  for surface-breaking faults (i.e., half the fault ellipse). The normal faults in the Caloris basin are clearly surface breaking, so we utilized the latter ratio for our analysis. A linear solution is obtained for constant aspect ratios. Best fits to the data along the linear portion of the relation are achieved with a constant aspect ratio of 2 (Figure 5), consistent with the range of fault aspect ratios on other terrestrial planets [Schultz et al., 2006]. By holding fault heights constant but increasing their lengths, the nonlinear analytical solution was calculated (Figure 5). When the nonlinear trends of the measurements and analytical solution match, it can be inferred that the continued growth of individual fault structures beyond the range over which the linear portion of the relation holds was restricted to that constant fault height.

[57] **Acknowledgments.** We thank the associate editor and two anonymous reviewers for helpful comments. CK also thanks Richard A. Schultz for sharing previously published work on confined fault growth. The MESSENGER project is supported by the NASA Discovery Program under contracts NASW-00002 to the Carnegie Institution of Washington and NAS5-97271 to The Johns Hopkins University Applied Physics Laboratory.

## References

- Balerski, J. A., S. A. Hauck II, P. Sun, C. Klimczak, P. K. Byrne, A. J. Dombard, O. S. Barnouin, M. T. Zuber, R. J. Phillips, and S. C. Solomon (2012), Tilted crater floors: Recording the history of Mercury's long-wavelength deformation, *Lunar Planet. Sci.*, 43, abstract 1850.

- Balcerski, J. A., S. A. Hauck II, P. Sun, C. Klimczak, P. K. Byrne, R. J. Phillips, and S. C. Solomon (2013), New constraints on timing and mechanisms of regional tectonism from Mercury's tilted craters, *Lunar Planet. Sci.*, 44, abstract 2444.
- Bieniawski, Z. T. (1989), *Engineering Rock Mass Classifications*, 251 pp, Wiley, New York.
- Bland, M. T., and W. B. McKinnon (2012), Forming Europa's folds: Strain requirements for the production of large-amplitude deformation, *Icarus*, 221, 694–709.
- Blewett, D. T., M. S. Robinson, B. W. Denevi, J. J. Gillis-Davis, J. W. Head, S. C. Solomon, G. M. Holsclaw, and W. E. McClintock (2009), Multispectral images of Mercury from the first MESSENGER flyby: Analysis of global and regional color trends, *Earth Planet. Sci. Lett.*, 285, 272–282, doi:10.1016/j.epsl.2009.02.021.
- Byrne, P. K., C. Klimczak, D. M. Blair, S. Ferrari, S. C. Solomon, A. M. Freed, T. R. Watters, and S. L. Murchie (2013), Tectonic complexity within volcanically infilled craters and basins on Mercury, *Lunar Planet. Sci.*, 44, abstract 1261.
- Cailleux, A. (1958), Etude quantitative de failles, *Rev. Géomorphologie Dynamique*, 9, 129–145.
- Cartwright, J. A., B. D. Trudgill, and C. S. Mansfield (1995), Fault growth by segment linkage: An explanation for scatter in maximum displacement and trace length data from the Canyonlands Grabens of SE Utah, *J. Struct. Geol.*, 17, 1319–1326, doi:10.1016/0191-8141(95)00033-A.
- Cavanaugh, J. F., et al. (2007), The Mercury Laser Altimeter instrument for the MESSENGER mission, *Space Sci. Rev.*, 131, 451–479, doi:10.1007/s11214-007-9273-4.
- Cowie, P. A., and C. H. Scholz (1992a), Displacement-length scaling relationship for faults: Data synthesis and discussion, *J. Struct. Geol.*, 14, 1149–1156.
- Cowie, P. A., and C. H. Scholz (1992b), Growth of faults by accumulation of seismic slip, *J. Geophys. Res.*, 97, 11,085–11,095.
- Cowie, P. A., and C. H. Scholz (1992c), Physical explanation for the displacement-length relationship of faults using a post-yield fracture mechanics model, *J. Struct. Geol.*, 14, 1133–1148, doi:10.1016/0191-8141(92)90065-5.
- Dawers, N. H., and M. H. Anders (1995), Displacement-length scaling and fault linkage, *J. Struct. Geol.*, 17, 607–614, doi:10.1016/0191-8141(94)00091-D.
- Dawers, N. H., M. H. Anders, and C. H. Scholz (1993), Growth of normal faults: Displacement-length scaling, *Geology*, 21, 1107–1110.
- Denevi, B. W., et al. (2013), The distribution and origin of smooth plains on Mercury, *J. Geophys. Res. Planets*, 118, 891–907, doi:10.1002/jgre.20075.
- Dombard, A. J., and S. A. Hauck II (2008), Despinning plus global contraction and the orientation of lobate scarps on Mercury: Predictions for MESSENGER, *Icarus*, 198, 274–276, doi:10.1016/j.icarus.2008.06.008.
- Elliott, D. (1976), The energy balance and deformation mechanisms of thrust sheets, *Phil. Trans. Roy. Soc. London, Ser. A*, 283, 289–312.
- Ernst, C. M., S. L. Murchie, O. S. Barnouin, M. S. Robinson, B. W. Denevi, D. T. Blewett, J. W. Head, N. R. Izenberg, S. C. Solomon, and J. H. Roberts (2010), Exposure of spectrally distinct material by impact craters on Mercury: Implications for global stratigraphy, *Icarus*, 209, 210–223, doi:10.1016/j.icarus.2010.05.022.
- Freed, A. M., S. C. Solomon, T. R. Watters, R. J. Phillips, and M. T. Zuber (2009), Could Pantheon Fossae be the result of the Apollodorus crater-forming impact within the Caloris basin, Mercury?, *Earth Planet. Sci. Lett.*, 285, 320–327, doi:10.1016/j.epsl.2009.02.038.
- Gillespie, P., J. J. Walsh, and J. Watterson (1992), Limitations of dimension and displacement data from single faults and the consequences for data analysis and interpretation, *J. Struct. Geol.*, 14, 1157–1172.
- Gupta, A., and C. H. Scholz (2000), A model of normal fault interaction based on observations and theory, *J. Struct. Geol.*, 22, 865–879, doi:10.1016/S0191-8141(00)00011-0.
- Hauck, S. A., II, A. J. Dombard, R. J. Phillips, and S. C. Solomon (2004), Internal and tectonic evolution of Mercury, *Earth Planet. Sci. Lett.*, 222, 713–728, doi:10.1016/j.epsl.2004.03.037.
- Hauck, S. A., II, et al. (2013), The curious case of Mercury's internal structure, *J. Geophys. Res. Planets*, 118, 1204–1220, doi:10.1002/jgre.20091.
- Hawkins, S. E., III, et al. (2007), The Mercury Dual Imaging System on the MESSENGER spacecraft, *Space Sci. Rev.*, 131, 247–338, doi:10.1007/s11214-007-9266-3.
- Head, J. W., et al. (2008), Volcanism on Mercury: Evidence from the first MESSENGER flyby, *Science*, 321, 69–72, doi:10.1126/science.1159256.
- Head, J. W., et al. (2009), Evidence for intrusive activity on Mercury from the first MESSENGER flyby, *Earth Planet. Sci. Lett.*, 285, 251–262, doi:10.1016/j.epsl.2009.03.008.
- Hoek, E., and E. T. Brown (1980), Empirical strength criterion for rock masses, *J. Geotech. Eng. Div. Am. Soc. Civil Eng.*, 106, 1030–1035.
- Irwin, G. R. (1962), Crack-extension force for a part-through crack in a plate, *J. Appl. Mech.*, 29, 651–654.
- Jaeger, J., N. G. Cook, and R. Zimmerman (2007), *Fundamentals of Rock Mechanics*, 4th ed., 593 pp., Blackwell, Oxford, U. K.
- Kassir, M. K., and G. C. Sih (1966), Three-dimensional stress distribution around an elliptical crack under arbitrary loadings, *J. Appl. Mech.*, 33, 601–611.
- King, S. D. (2008), Pattern of lobate scarps on Mercury's surface reproduced by a model of mantle convection, *Nat. Geosci.*, 1, 229–232.
- Klimczak, C., R. A. Schultz, and A. L. Nahm (2010), Evaluation of the origin hypotheses of Pantheon Fossae, central Caloris basin, Mercury, *Icarus*, 209, 262–270, doi:10.1016/j.icarus.2010.04.014.
- Klimczak, C., T. R. Watters, C. M. Ernst, A. M. Freed, P. K. Byrne, S. C. Solomon, D. M. Blair, and J. W. Head (2012), Deformation associated with ghost craters and basins in volcanic smooth plains on Mercury: Strain analysis and implications for plains evolution, *J. Geophys. Res.*, 117, E00L03, doi:10.1029/2012JE004100.
- Manighetti, I., G. C. P. King, and Y. Gaudemer (2001), Slip accumulation and lateral propagation of active normal faults in Afar, *J. Geophys. Res.*, 106, 13,667–13,696.
- McAdoo, D. C., and D. T. Sandwell (1985), Folding of oceanic lithosphere, *J. Geophys. Res.*, 90, 8563–8569, doi:10.1029/JB090iB10p08563.
- Melosh, H. J., and W. B. McKinnon (1988), The tectonics of Mercury, in *Mercury*, edited by F. Vilas, C. R. Chapman, and M. S. Matthews, pp. 374–400, University of Arizona Press, Tucson, Ariz.
- Michel, N. C., S. A. Hauck II, S. C. Solomon, R. J. Phillips, J. H. Roberts, and M. T. Zuber (2013), Thermal evolution of Mercury as constrained by MESSENGER observations, *J. Geophys. Res. Planets*, 118, 1033–1044, doi:10.1002/jgre.20049.
- Montésí, L. G. J., and M. T. Zuber (2003), Spacing of faults at the scale of the lithosphere and localization instability: 1. Theory, *J. Geophys. Res.*, 108(B2), 2110, doi:10.1029/2002JB001923.
- Murchie, S. L., et al. (2008), Geology of the Caloris basin, Mercury: A view from MESSENGER, *Science*, 321, 73–76, doi:10.1126/science.1159261.
- Murray, B. C., R. G. Strom, N. J. Trask, and D. E. Gault (1975), Surface history of Mercury: Implications for terrestrial planets, *J. Geophys. Res.*, 80, 2508–2514.
- Neumann, G. A., and M. T. Zuber (1995), A continuum approach to the development of normal faults, in *Rock Mechanics: Proceedings of the 35th U.S. Symposium on Rock Mechanics*, edited by J. K. Daemen and R. A. Schultz, pp. 191–198, Balkema Publishers, Rotterdam, The Netherlands.
- Oberst, J., F. Preusker, R. J. Phillips, T. R. Watters, J. W. Head, M. T. Zuber, and S. C. Solomon (2010), The morphology of Mercury's Caloris basin as seen in MESSENGER stereo topographic models, *Icarus*, 209, 230–238, doi:10.1016/j.icarus.2010.03.009.
- Peacock, D. C. P., and D. J. Sanderson (1994), Geometry and development of relay ramps in normal fault systems, *Amer. Assoc. Petro. Geol. Bull.*, 78, 147–165.
- Polit, A. T., R. A. Schultz, and R. Soliva (2009), Geometry, displacement-length scaling, and extensional strain of normal faults on Mars with inferences on mechanical stratigraphy of the Martian crust, *J. Struct. Geol.*, 31, 662–673, doi:10.1016/j.jsg.2009.03.016.
- Preusker, F., J. Oberst, J. W. Head, T. R. Watters, M. S. Robinson, M. T. Zuber, and S. C. Solomon (2011), Stereo topographic models of Mercury after three MESSENGER flybys, *Planet. Space Sci.*, 59, 1910–1917, doi:10.1016/j.pss.2011.07.005.
- Ricard, Y., and C. Froidevaux (1986), Stretching instabilities and lithospheric boudinage, *J. Geophys. Res.*, 91, 8314–8324.
- Roberts, J. H., and O. S. Barnouin (2012), The effect of the Caloris impact on the mantle dynamics and volcanism of Mercury, *J. Geophys. Res.*, 117, E02007, doi:10.1029/2011JE003876.
- Robinson, M. S., et al. (2008), Reflectance and color variations on Mercury: Regolith processes and compositional heterogeneity, *Science*, 321, 66–69, doi:10.1126/science.1160080.
- Rubin, A. M. (1990), A comparison of rift-zone tectonics in Iceland and Hawaii, *Bull. Volcanol.*, 52, 302–319, doi:10.1007/BF00304101.
- Schlische, R. W., S. S. Young, R. V. Ackermann, and A. Gupta (1996), Geometry and scaling relations of a population of very small rift-related normal faults, *Geology*, 24, 683–686.
- Scholz, C. H. (1997), Earthquake and fault populations and the calculation of brittle strain, *Geowissenschaften*, 15, 124–130.
- Scholz, C. H. (2002), *The Mechanics of Earthquakes and Faulting*, 471 pp., Cambridge University Press, Cambridge.
- Scholz, C. H., N. H. Dawers, J. Z. Yu, M. H. Anders, and P. A. Cowie (1993), Fault growth and fault scaling laws: Preliminary results, *J. Geophys. Res.*, 98, 21,951–21,961.
- Schultz, R. A. (1996), Relative scale and the strength and deformability of rock masses, *J. Struct. Geol.*, 18, 1139–1149, doi:10.1016/0191-8141(96)00045-4.
- Schultz, R. A. (2000), Fault-population statistics at the Valles Marineris extensional province, Mars: Implications for segment linkage, crustal strains, and its geodynamical development, *Tectonophysics*, 316, 169–193.

- Schultz, R. A. (2003), A method to relate initial elastic stress to fault population strains, *Geophys. Res. Lett.*, 30(11), 1593, doi:10.1029/2002GL016681.
- Schultz, R. A., and H. Fossen (2002), Displacement-length scaling in three dimensions: The importance of aspect ratio and application to deformation bands, *J. Struct. Geol.*, 24, 1389–1411.
- Schultz, R. A., C. H. Okubo, and S. Wilkins (2006), Displacement-length scaling relations for faults on the terrestrial planets, *J. Struct. Geol.*, 28, 2182–2193, doi:10.1016/j.jsg.2006.03.034.
- Schultz, R. A., R. Soliva, H. Fossen, C. H. Okubo, and D. M. Reeves (2008), Dependence of displacement-length scaling relations for fractures and deformation bands on the volumetric changes across them, *J. Struct. Geol.*, 30, 1405–1411, doi:10.1016/j.jsg.2008.08.001.
- Schultz, R. A., R. Soliva, C. H. Okubo, and D. Mege (2010), Fault populations, in *Planetary Tectonics*, edited by T. R. Watters and R. A. Schultz, pp. 457–510, Cambridge University Press, Cambridge.
- Smith, D. E., et al. (2012), Gravity field and internal structure of Mercury from MESSENGER, *Science*, 336, 214–217, doi:10.1126/science.1218809.
- Soliva, R., and A. Benedicto (2004), A linkage criterion for segmented normal faults, *J. Struct. Geol.*, 26, 2251–2267, doi:10.1016/j.jsg.2004.06.008.
- Soliva, R., and A. Benedicto (2005), Geometry, scaling relations and spacing of vertically restricted normal faults, *J. Struct. Geol.*, 27, 317–325, doi:10.1016/j.jsg.2004.08.010.
- Soliva, R., R. A. Schultz, and A. Benedicto (2005), Three-dimensional displacement-length scaling and maximum dimension of normal faults in layered rocks, *Geophys. Res. Lett.*, 32, L16302, doi:10.1029/2005GL023007.
- Soliva, R., A. Benedicto, and L. Maerten (2006), Spacing and linkage of confined normal faults: Importance of mechanical thickness, *J. Geophys. Res.*, 111, B01402, doi:10.1029/2004JB003507.
- Soliva, R., A. Benedicto, R. A. Schultz, L. Maerten, and L. Micarelli (2008), Displacement and interaction of normal fault segments branched at depth: Implications for fault growth and potential earthquake rupture size, *J. Struct. Geol.*, 30, 1288–1299, doi:10.1016/j.jsg.2008.07.005.
- Solomon, S. C., C. Klimczak, P. K. Byrne, S. A. Hauck II, J. A. Balcerski, A. J. Dombard, M. T. Zuber, D. E. Smith, R. J. Phillips, J. W. Head, and T. R. Watters (2012), Long-wavelength topographic change on Mercury: Evidence and mechanisms, *Lunar Planet. Sci.*, 43, abstract 1578.
- Strom, R. G., N. J. Trask, and J. E. Guest (1975), Tectonism and volcanism on Mercury, *J. Geophys. Res.*, 80, 2478–2507.
- Thomas, P. G., P. Masson, and L. Fleitout (1988), Tectonic history of Mercury, in *Mercury*, edited by F. Vilas, C. R. Chapman, and M. S. Matthews, pp. 401–428, University of Arizona Press, Tucson, Ariz.
- Trask, N. J., and J. E. Guest (1975), Preliminary geologic terrain map of Mercury, *J. Geophys. Res.*, 80, 2461–2477.
- Turcotte, D. L., and G. Schubert (2002), *Geodynamics*, 2nd ed., 456 pp., Cambridge University Press, Cambridge.
- Walsh, J. J., and J. Watterson (1988), Analysis of the relationship between displacements and dimensions of faults, *J. Struct. Geol.*, 10, 239–247, doi:10.1016/0191-8141(88)90057-0.
- Watters, T. R., and F. Nimmo (2010), The tectonics of Mercury, in *Planetary Tectonics*, edited by T. R. Watters and R. A. Schultz, pp. 15–80, Cambridge University Press, Cambridge.
- Watters, T. R., M. S. Robinson, and A. C. Cook (1998), Topography of lobate scarps on Mercury: New constraints on the planet's contraction, *Geology*, 26, 991–994.
- Watters, T. R., F. Nimmo, and M. S. Robinson (2005), Extensional troughs in the Caloris basin of Mercury: Evidence of lateral crustal flow, *Geology*, 33, 669–672, doi:10.1130/G21678.1.
- Watters, T. R., S. C. Solomon, M. S. Robinson, J. W. Head, S. L. André, S. A. Hauck II, and S. L. Murchie (2009a), The tectonics of Mercury: The view after MESSENGER's first flyby, *Earth Planet. Sci. Lett.*, 285, 283–296, doi:10.1016/j.epsl.2009.01.025.
- Watters, T. R., S. L. Murchie, M. S. Robinson, S. C. Solomon, B. W. Denevi, S. L. André, and J. W. Head (2009b), Emplacement and tectonic deformation of smooth plains in the Caloris basin, Mercury, *Earth Planet. Sci. Lett.*, 285, 309–319, doi:10.1016/j.epsl.2009.03.040.
- Watters, T. R., S. C. Solomon, C. Klimczak, A. M. Freed, J. W. Head, C. M. Ernst, D. M. Blair, T. A. Goudge, and P. K. Byrne (2012), Extension and contraction within volcanically buried impact craters and basins on Mercury, *Geology*, 40, 1123–1126, doi:10.1130/G33725.1.
- Watterson, J. (1986), Fault dimensions, displacements and growth, *Pure Appl. Geophys.*, 124, 365–373, doi:10.1007/BF00875732.
- Weider, S. Z., L. R. Nittler, R. D. Starr, T. J. McCoy, K. R. Stockstill-Cahill, P. K. Byrne, B. W. Denevi, J. W. Head, and S. C. Solomon (2012), Chemical heterogeneity on Mercury's surface revealed by the MESSENGER X-Ray Spectrometer, *J. Geophys. Res.*, 117, E00L05, doi:10.1029/2012JE004153.
- Wessel, P., and W. H. Smith (1998), New, improved version of Generic Mapping Tools released, *Eos Trans. Am. Geophys. Un.*, 79(47), 579.
- Wieczorek, M. A., et al. (2013), The crust of the Moon as seen by GRAIL, *Science*, 339, 671–675, doi:10.1126/science.1231530.
- Wilkins, S. J., and R. A. Schultz (2005), 3D cohesive end-zone model for source scaling of strike-slip interplate earthquakes, *Bull. Seismol. Soc. Am.*, 95, 2232–2258, doi:10.1785/0120020106.
- Willemse, E. J. M. (1997), Segmented normal faults: Correspondence between three-dimensional mechanical models and field data, *J. Geophys. Res.*, 102, 675–692.
- Willemse, E. J. M., D. D. Pollard, and A. Aydin (1996), Three-dimensional analyses of slip distributions on normal fault arrays with consequences for fault scaling, *J. Struct. Geol.*, 18, 295–309, doi:10.1016/S0191-8141(96)80051-4.
- Wyrick, D. Y., A. P. Morris, and A. A. Ferrill (2011), Normal fault growth in analog models and on Mars, *Icarus*, 212, 559–567, doi:10.1016/j.icarus.2011.01.011.
- Zuber, M. T. (1987), Compression of oceanic lithosphere: An analysis of intraplate deformation in the Central Indian Basin, *J. Geophys. Res.*, 92, 4817–4825.
- Zuber, M. T., et al. (2012), Topography of the northern hemisphere of Mercury from MESSENGER laser altimetry, *Science*, 336, 217–220, doi:10.1126/science.1218805.